

PAPER

## Multi-image oil-film interferometry skin friction measurements

To cite this article: J W Naughton and M D Hind 2013 *Meas. Sci. Technol.* **24** 124003

View the [article online](#) for updates and enhancements.

### You may also like

- [The ratioed image film thickness meter](#)  
Nicholas M Husen, Tianshu Liu and John P Sullivan
- [Numerical simulation of bubble changes in an oil film impacted by oil droplets via a coupled level set and volume-of-fraction method](#)  
Jian-hong Zhou, Bao-hong Tong, Wei Wang et al.
- [Hybrid oil film approach to measuring skin friction distribution](#)  
Mitsuru Kurita and Hidetoshi Iijima



**NOW WITH MICROPL UPGRADE  
FOR SPECTRAL AND TIME-RESOLVED  
PHOTOLUMINESCENCE MICROSCOPY.**



**edinst.com**

# Multi-image oil-film interferometry skin friction measurements

J W Naughton and M D Hind

Department of Mechanical Engineering, University of Wyoming, Laramie, WY 82071, USA

E-mail: [naughton@uwyo.edu](mailto:naughton@uwyo.edu)

Received 10 April 2013, in final form 15 August 2013

Published 22 October 2013

Online at [stacks.iop.org/MST/24/124003](http://stacks.iop.org/MST/24/124003)

## Abstract

The benefits of analyzing multiple interferogram images obtained using oil-film interferometry in order to determine wall shear stress are assessed. Both dual- and multi-image analysis approaches are implemented and compared to standard single interferogram approaches. Each of the analysis approaches is derived from the thin oil-film equation. To assess the different implementations, both experimental interferograms and simulated oil films are used. The simulations determine the oil-film height as a function of space and time by solving the thin oil-film equation subject to a known wall shear stress distribution, whereas experimental interferograms were obtained in a turbulent flat plate boundary layer. The results of analyzing these data with the three different analysis approaches suggest that they all work equally well when test conditions are approximately steady. For tunnels with long transients at startup or when multiple test conditions need to be measured in a single run, the multi-image approach is recommended.

**Keywords:** wall shear stress, skin friction, interferometry, thin oil film

(Some figures may appear in colour only in the online journal)

## 1. Introduction

In wall bounded flows, a critical parameter is the wall shear stress. It serves as an important scaling quantity when trying to understand the fundamental physics of the near-wall behavior of such flows. However, wall shear stress is also a critical measurement for practical applications as it provides a measurement of the viscous drag. Wall shear stress is also considered important for validation of simulations of wall-bounded flows as it is very sensitive to the near-wall flow physics. Although wall shear stress has long been considered a difficult quantity to measure accurately, the number of reported wall shear stress measurements has grown steadily over the last two decades. Of the techniques used to measure wall shear stress, oil-film interferometry has become popular due to its accuracy and limited equipment requirements.

Oil-film interferometry has been developed over the past several decades, changing in its implementation as imaging technology improved. Details of this development are given, for example, by Naughton and Sheplak [1]. The basis for the instrument was developed by Squire in 1962 [2] when equations were developed to describe the behavior of an oil

film when acted upon by surface shear stress. Squire's intent was to show that oil followed local surface streamlines, but the equations provided a means of determining wall shear stress. In response to the challenge of measuring the thickness of oil films that was only microns thick, Tanner and his students (see, for example, [3]) demonstrated the use of interferometry. Although Tanner and students demonstrated that the spatial interference pattern could be recorded with a camera, the difficulty of working with image data at this time led to the development of point techniques that used the time history of the interference pattern. Although point techniques worked reasonably well, the method was tedious to use as only a single point was normally captured in each test. With the advent of inexpensive CCD cameras, image based approaches were again viable. Although sampling along a line at various times was investigated [4], single-image approaches became the standard approach (see, for example, [5]). The attractiveness of such approaches was that information from multiple points on a body's surface could be gained during a single run. Since the introduction of the approach, improvements have been steadily made including the determination of the skin friction distribution from a single oil-film pattern [6] to application of

photogrammetry methods that provide the camera-to-physical space transformations [7] required for determining shear stress from interferograms. As the tools available for processing interferograms improved and demonstrations of the technique were successful, the measurement of wall shear stress via oil-film interferometry has been applied to a wide range of flows. Boundary layers on flat plates [8] and airfoils [9], separated flows [10], wall jets [11], and impinging jets [12] represent some examples of the flows in which oil-film interferometry has been used. Although most applications of oil-film interferometry have been in smaller laboratory flows, its use has been demonstrated in large wind tunnels [13] and in flight test [14].

Most of the applications of oil-film interferometry have used the single-image approach, whereas simultaneous use of spatial and temporal variations of the oil-film height has received relatively little attention. Siller *et al* [4] and Fernholz *et al* [15] used both spatial and temporal information along a line along with a one-dimensional version of the oil-film equation to determine the wall shear stress, with some of the approaches yielding spatially-varying wall shear stress. Similarly, Naughton and Brown [16] used both temporal and spatial data to determine wall shear stress. The height over a region of interest was determined at two different times and used with the oil-film equation to determine wall shear stress. By using two-dimensional spatial information, a greater region of the model was investigated. However, the demands on the quality of the interferograms for this approach make it very difficult to implement in practice. Driver and Drake demonstrated that, using interferograms taken at multiple times, variations in conditions during a test could be addressed [17]. Despite these investigations, there is still much to explore in order to take full advantage of the additional data provided by images of the interferogram taken at multiple times.

The objective of the current work is to implement single- and multiple-interferogram analysis approaches capable of measuring spatially varying wall shear stress and to evaluate their relative strengths and weaknesses. The focus here is on methods that analyze lines of data extracted from interferograms, as such approaches have been most common in actual tests. In addition, the extension of the conclusions drawn from the approaches investigated here to methods that analyze regions of a surface is reasonable. The past poor performance of multiple-image approaches for determining spatially varying wall shear stress (e.g. [18]) is also considered. To accomplish these objectives, both simulated and experimental data were used. The simulated data were generated using a Falkner–Skan flow over a 30° wedge, whereas the experiment considered a turbulent flat plate flow. To fully explore the different methods' capabilities, both simulation and experiment considered flows that were steady and flows that varied with time. Single-, dual-, and multiple-image approaches applied to simulated interferograms demonstrated that all approaches work equally well under ideal, steady conditions. Two or multiple-image approaches worked better for cases that see changes in conditions during a run. These encouraging results were also demonstrated when the approaches were applied to experimental interferograms, even

though the experimental interferograms exhibited many flaws typical of experimental data.

The remainder of the paper is organized as follows. First, a description of oil-film interferometry is provided including the theoretical basis for the instrument, solution of the thin oil-film equation, experimental implementation, and the analysis of the experimental and computational data. The results of applying the different analysis approaches are then presented and discussed before drawing some conclusions concerning the applicability of the approaches.

## 2. Description

The ability to determine wall shear stress from a thin oil film is based upon the thin oil-film equation. This equation is first discussed, and then simulating oil films as well as measuring wall shear stress using interferograms is considered. Finally, the different analysis approaches are discussed relative to their application to computational and experimental data.

### 2.1. OFI theory

Squire first developed the thin oil-film equation to determine if oil flow visualization commonly used in wind tunnels at that time revealed surface streamline patterns accurately [2]. The one-dimensional form used here (see [19] for a full derivation) relates the wall shear stress  $\tau_w$  to the oil-film thickness  $h$  and the oil dynamic viscosity  $\mu$ ,

$$\frac{\partial h}{\partial t} + \frac{\partial}{\partial x} \left( \frac{\tau_{w,x} h^2}{2\mu} \right) = 0, \quad (1)$$

where  $x$  is the spatial coordinate and  $t$  is time. As evident from the equation, if the wall shear stress and oil properties are known, the height of the oil as a function of time may be determined (the direct solution). Conversely, the equation suggests that, if the height is known as a function of time and space, the wall shear stress may be determined (the inverse solution).

Tanner and his co-workers were the first to realize the potential instrument suggested by the thin oil-film equation. To measure the oil-film height, they suggested using interferometry (for example, see [3]). As shown in figure 1(b), light striking the thin film surface partially reflects from and partially transmits through the oil. The light passing through the oil strikes a reflective surface and reflects back upward through the oil. The two light beams exiting the oil have a phase difference due to the difference in the path lengths. Depending on the phase difference, the two beams can constructively or destructively interfere as shown in figure 1(c) producing the bright or dark intensities shown in figure 1(a). Knowing the location of the oil leading edge, fringe counting is used to determine the phase difference  $\phi$  at different locations in the film. Using optical relationships, it can be shown that, for an illumination wavelength  $\lambda$ , the oil height  $h$  is related to the phase difference  $\phi$ :

$$h = \frac{\lambda \phi}{4\pi} \left( \frac{1}{\sqrt{n_f^2 - n_a^2 \sin^2 \theta_i}} \right), \quad (2)$$

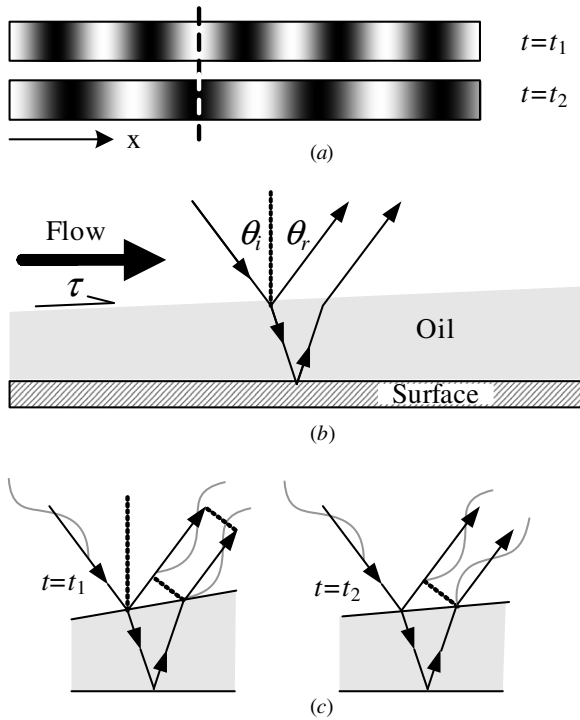


**Figure 1.** Interference in a thin film: (a) interference patterns at two times, (b) path length difference between light reflected at two interfaces, and (c) constructive and destructive interference.

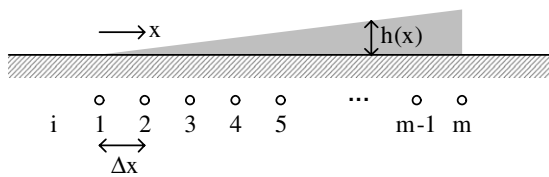


**Figure 2.** One-dimensional computational grid associated with an oil film.

where  $\theta_i$  is the local illumination incidence angle, and  $n_f$  and  $n_a$  are the indices of refraction of the oil and air, respectively [20, 21].

## 2.2. Solution of the thin oil-film equation

As alluded to above, there are two solutions approaches for the thin oil-film equation that are of interest here: the direct and inverse solutions. In the direct solution, a given wall shear stress and oil properties are used with (1) to determine the height of the oil as a function of time. Consider an oil film with an associated one-dimensional grid as shown in figure 2. For shear stress that varies in space but is constant in time, Brown and Naughton [19] give several different means of discretizing equation (1). The one-dimensional equivalent of the box-implicit method they discuss is given by

$$h_i^{n+1} = \frac{h_i^n + (h^n - h^{n+1})_{i-1} + \frac{\Delta t}{\Delta x} (\tau h^n h^{n+1} / \mu)_{i-1}}{1 + \frac{\Delta t}{\Delta x} (\tau h^n / \mu)_i}, \quad (3)$$

where the superscripts identify the time level, the subscripts indicate the spatial location, and  $\Delta x$  and  $\Delta t$  represent the node separation and time step, respectively. Assuming that an initial condition of the oil is known, the solution at  $t + \Delta t$  can

be swept downstream in space from the leading edge ( $i = 1$ ) where  $h = 0$ . Subsequent time steps are performed in a similar way but using the updated oil-film height. This is the form of the equation that will be used to determine the oil-film height given a wall shear stress field.

When the oil-film height and oil properties are known and the wall shear stress is desired, the inverse solution approach must be used. For this study, single-, dual-, and multiple-image approaches were implemented. A necessary assumption for the single-image approach is that the oil film is subject to a steady wall shear stress from the time the oil film is first exposed to the flow. This essential assumption is the same used for all single-image approaches and affects the applicability of the approach. Typically, the solution is cast in terms of skin friction coefficient  $C_f = \tau_w / (q)$ , where  $q$  is dynamic pressure. Skin friction is used as it varies less than the wall shear stress as test conditions change. Assuming constant skin friction, Brown and Naughton [19] showed that, for wall shear stress varying only with  $x$ , (1) simplifies to

$$\frac{\partial}{\partial x} (C_f h^2) - 2h \int_0^t \frac{q}{\mu} dt = 0, \quad (4)$$

where  $C_f$  is the skin friction coefficient and  $q$  is a reference dynamic pressure. The reference dynamic pressure may be taken at any location that tracks the flow's evolution, and the resulting skin friction coefficient will be based on this reference value. This equation may be numerically solved for node points along the extracted line using central differences. For a general node, the solution becomes

$$C_{f,i+1} = C_{f,i} \frac{h_i^2}{h_{i+1}^2} + \frac{h_{i+1} + h_i}{h_{i+1}^2} \Delta x \int_0^t \frac{q}{\mu} dt, \quad (5)$$

where  $i$  is the node number. Knowing the skin friction coefficient at node 2, the solution is simply marched downstream to determine the skin friction coefficient for nodes  $i > 1$ . For  $i = 1$ ,  $h_1 = 0$  and the result simplifies to

$$C_{f,2} = \frac{\Delta x}{h_{i=2}} \int_0^t \frac{q}{\mu} dt, \quad (6)$$

which is the constant shear stress solution.

When multiple oil-film interferograms from a single test are available, the assumption of constant shear over the entire run is no longer required. Instead, the flow is only assumed to be steady over the interval analyzed, and the solution is now cast in terms of wall shear stress instead of skin friction coefficient. The additional data may also be used to more accurately evaluate some terms and smooth the raw data if necessary. Starting with (1) and assuming the wall shear stress is only a function of  $x$ , the equation is integrated between times where the data are to be analyzed:

$$\underbrace{h(t_2) - h(t_1)}_B + \frac{\partial}{\partial x} \frac{\tau}{2} \underbrace{\int_{t_1}^{t_2} \frac{h^2}{\mu} dt}_A = 0, \quad (7)$$

where  $A$  indicates the time integral and  $B$  represents the height change over the time interval at a given location. As above, this equation is solved numerically using central differences yielding

$$\tau_{i+1} = 2\Delta x (\tau_i A_i - B_{i+1/2}) / A_{i+1}. \quad (8)$$

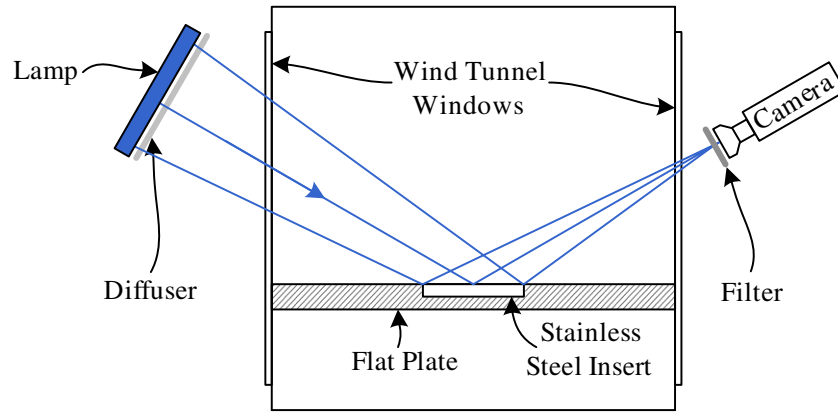


**Figure 3.** Wind tunnel with flat plate and oil-film interferometry setup used in the present study.

For  $i = 1$ ,  $A_1$  becomes zero, and the equation simplifies to

$$\tau_{i=2} = -2\Delta x B_{1/2}/A_2. \quad (9)$$

Once  $\tau_{i=2}$  is determined, the solution is simply marched downstream using (8). The primary difference between the dual-image and multiple-image approaches is how term  $A$  is evaluated. For the dual-image approach, the integral is approximated using the height values at the endpoints of the time interval being analyzed, whereas the multiple-image approach uses data from several times between the endpoints to evaluate the integral.

Although the dual- and multiple-image approaches appear to offer better accuracy, there are some drawbacks in their use. Capturing interferograms during a run requires optical access, and there is significantly more data to obtain and process. In return, the assumption of steady wall shear stress over the entire run is no longer necessary as it is for single-image approaches. This makes the dual- and multiple-image techniques immune to facility startup and shut-down effects and also allows the analysis of interferograms that have been exposed to more than one steady run condition.

### 2.3. Experimental setup and data acquisition

To fully test the different analysis approaches, both experiment and simulations that could be used to test the results were necessary. In this section, the experimental setup is discussed. The tests were conducted in a low speed wind tunnel with  $0.3 \text{ m} \times 0.3 \text{ m}$  test section cross section. As shown in figure 3, a flat plate that spanned the test section was mounted in the tunnel. The leading edge of the plate (not shown in the figure) had a modified elliptical shape to avoid separation. The flow was tripped near the leading edge such that, at the test location (approximately  $0.95 \text{ m}$  behind the leading edge), the boundary layer was fully turbulent. For performing oil-film interferometry, the model could accommodate  $0.20 \text{ m} \times 0.20 \text{ m}$  inserts, which in this case were polished stainless steel plates.

Interference patterns were created in the oil films applied to the surface using the hardware shown in figure 3. An extended light source provided by a mercury lamp passed through a diffuser and illuminated the model. Light reflected from both the oil/air and oil/stainless steel interfaces. The

reflected light passed through a notch filter that allowed only the  $435.8 \text{ nm}$  line from the mercury lamp to pass into the camera where images of the resulting interferogram were captured.

To capture interferogram images that could be processed for wall shear stress, a standard approach was used to ensure all data necessary were available. First, a two step calibration of the camera/lens system was performed such that a pixel location in camera space determined both the physical location on the model and the local illumination angle  $\theta_i$ . A three-dimensional step model and a small grid placed on the model were used for this calibration procedure, which is discussed in detail in [7]. Once the calibration was complete, 20 cSt silicone oil was applied to the model. The data acquisition program used to capture images as well as test conditions (dynamic pressure and plate temperature) was then enabled followed by startup of the tunnel. Images were acquired over a 40 min period of time with a 10 s time separation between images for the cases tested here. Typical interferograms captured during a test are shown in figure 4.

### 2.4. Simulation and experimental cases

In order to fully demonstrate the ability of the different analysis processes under different conditions, data obtained from several experimental and computational cases were considered. The two simulation cases used here were both based on a Falkner–Skan wedge flow [22] generated by a boundary layer edge velocity  $U_e$  given by  $U_e = Kx^m$ , where  $K$  governs the magnitude of the velocity, and  $m$  is an exponent that is related to the wedge angle. For the  $30^\circ$  (included angle) wedge investigated here, the value of the exponent  $m$  was  $0.0909$ . It can be shown that this flow results in a skin friction coefficient distribution given by

$$C_f = 0.9673 Re^{-1/2}, \quad (10)$$

where  $Re = U_e x / \nu$ , where  $\nu$  is the kinematic viscosity of air. For the first case (case 1C),  $K$  was set to 30 throughout the simulation yielding a constant wall shear stress. In the second case (case 2C),  $K$  initially started out as 30 and increased abruptly to 45 at 300 s into the simulation. Both simulations were carried out for a period of 500 s.



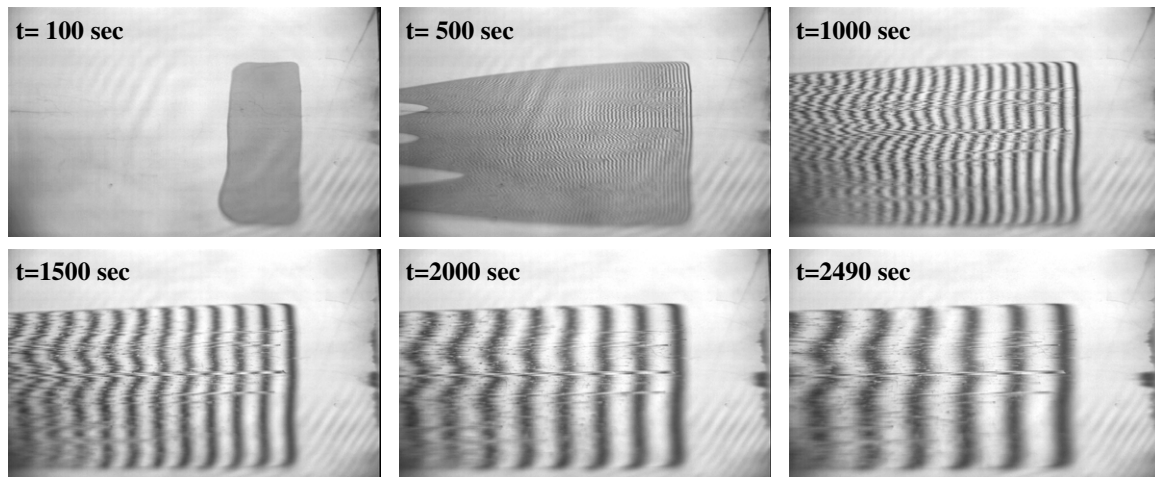


**Figure 4.** Interferograms produced by a thin oil film captured during a single run in a wind tunnel.

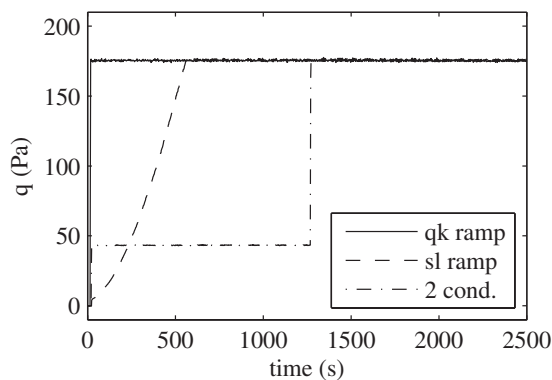


**Figure 5.** Dynamic pressure histories for the three experimental cases tested: quick ramp (case 1E), slow ramp (case 2E), and two-condition case (case 3E).

Experiments were conducted under three conditions: a quick startup with constant run condition thereafter (case 1E), a slow startup with constant run conditions thereafter (case 2E), and a quick startup with a constant run condition followed by a rapid change to another constant run condition (case 3E). For the first two cases, the free-stream velocity at test conditions was  $19.4 \text{ m s}^{-1}$  corresponding to a dynamic pressure of 175 Pa. In the third case, the tunnel was first run at a free-stream velocity of  $9.6 \text{ m s}^{-1}$  corresponding to a dynamic pressure of 43 Pa and later increased to  $19.4 \text{ m s}^{-1}$ . Figure 5 shows the dynamic pressure during the run demonstrating the very different flow conditions for the different cases. Both experimental and computational test cases are summarized in table 1.

### 2.5. Computational analysis

To obtain simulations of oil-film height under different wall shear stress conditions, the direct solution of the oil-film equation (1) discussed above was used. These simulations provided a known solution that could be used to assess the different analysis approaches. The Falkner–Skan solution for a wedge having a  $30^\circ$  included angle discussed above was used for this analysis. This flow produced a significant acceleration

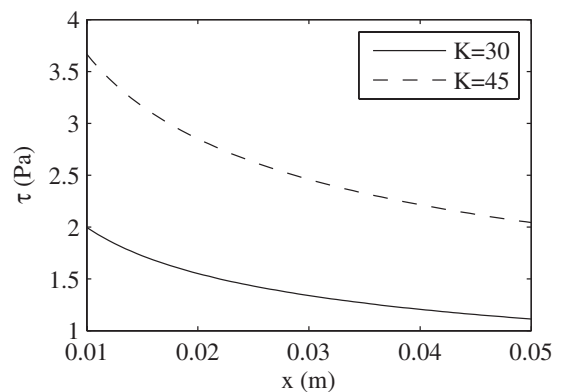


**Figure 6.** Shear stress distributions for the cases tested: case 1C only uses the lower wall shear stress solution throughout the simulation, whereas case 2C uses the lower wall shear stress solution for the first 300 s, and the higher value for the next 200 s.

**Table 1.** Experimental and computational cases used for assessing different oil-film interferometry analysis approaches.

Case	Type	Description
1C	Computation	Falkner–Skan wedge flow, single constant shear stress level
2C	Computation	Falkner–Skan wedge flow, two different shear stress levels
1E	Experiment	Boundary layer, single shear stress level, short startup
2E	Experiment	Boundary layer, single shear stress level, long startup
3E	Experiment	Boundary layer, two different shear stress levels

of the flow with a corresponding variation of the wall shear stress. For one simulation, case 1C, the wall shear stress varied in space, but not in time. In contrast, a step change in the shear stress magnitude by increasing the value of  $K$  was imposed part way through the second simulation, case 2C. The two wall shear stress distributions are shown in figure 6: case 1 used only the lower curve, whereas case 2 started out with the lower curve and transitioned to the higher curve at 300 s. Using these shear stress distributions, the oil-film height was determined

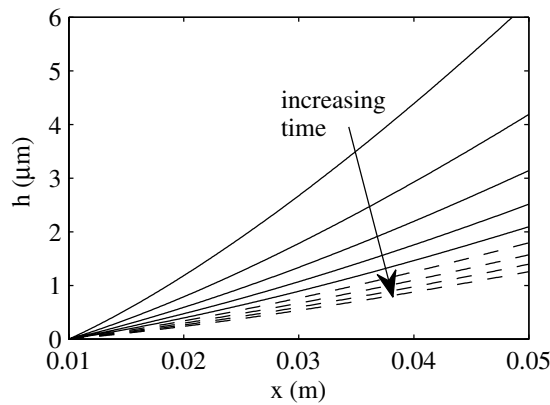


**Figure 7.** Oil-film heights predicted by the direct solver when 20 cSt oil was acted upon by the shear stress distribution for case 2C. The results show the height distribution for 9 different times starting at 100 s (the thickest oil-film height shown) with 50 s separation (the height decreasing for each time shown). The solid lines indicate times when the wall shear stress was at the first level, and the dashed lines indicate when the wall shear stress had changed to the second level.

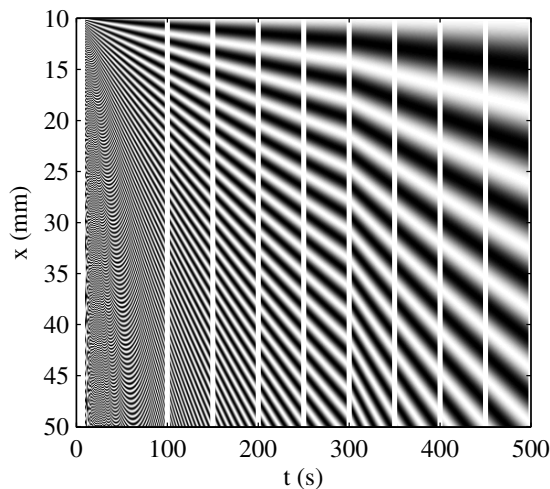


**Figure 8.** Interferogram calculated for the shear stress distribution of case 2C. The time where the shear stress changes (300 s) is quite obvious in this figure. The white lines in the figure correspond to the times where the height is shown in figure 7.

for a 500 s period using the direct solution approach (3). The resulting height distribution for case 2 is shown in figure 7. The height is first shown at 100 s into the simulation (the top curve) and then every 50 s thereafter. Note that the rate at which the height changes decreases as time goes on even though the wall shear stress increases.

Knowing the height spatial distribution at different times, the phase at those different times was calculated using (2), from which the interference pattern could be determined. As an observer, one would observe the fringe spacing slowly growing. To visualize the changes in the interference pattern with time, the intensity distribution that would be observed at different times was generated. The result is the intensity pattern in figure 8. Although the shear stress change at 300 s in case 2 is difficult to see in figure 7, it is quite easily spotted in the interferogram where the slope of the constant phase lines

(e.g. the brightest white and the deepest black) change as soon as the shear stress changes. With height distributions such as those in figure 7, the different processing algorithms discussed in section 2.2 were tested.

## 2.6. Experimental analysis

Before discussing the results of analyzing the simulated height distributions, it is important to discuss the analysis required to determine skin friction from the experimental data. The multi-image analysis approach is discussed first followed by descriptions of the one and two image approaches. Equation (2) indicates that, if the phase data can be determined from the interferograms, it is straightforward to calculate the oil height. Once the oil height is known, the same inverse solution approaches applied to the computational data can be used to determine wall shear stress from the experimental data. The processing approach initially follows that discussed by Naughton *et al* [10] and Naughton and Liu [7] and is briefly summarized here. Calibration images acquired as discussed above were used to calibrate the lens/camera system in model space using photogrammetry. A line parallel to the flow direction was then chosen for analysis. This same line was extracted from all interferograms taken during the test. Figures 9 and 10 show the results for constant wall shear stress (case 1E) and for two different wall shear stresses (case 3E), respectively. Figures 9 and 10(a) show an example original interferogram (snapshot of the interference pattern at one time) with a line indicating where the data was extracted for all times. Additionally, figures 9 and 10(b) show the extracted intensities as a function of time. The spatio-temporal behavior of the oil films is evident in these figures. For example, the constant shear stress case (case 1E) exhibits nearly linear lines of constant phase, whereas the case with varying shear stress shows a distinct change in slope at  $\sim 1300$  Section. The latter case is very similar to the simulation results for two shear stresses (case 2C) shown in 8.

To extract phase from the interference patterns, a correlation-based approach [10] was used to identify the maxima and minima of the interferograms. The points so extracted are shown in figure 11(a). Since the phase of these points was known, the oil-film height shown in figure 11(b) could be calculated using (2). To take advantage of the data provided by considering lines from multiple interferograms, the locations of intensity minima and maxima were linearly fit against time. A linear curve fit was chosen as the lines of constant phase did not vary over a very large distance, and the shear stress was approximately constant over the spatial extent of the data considered. The results of fitting the data are shown in figure 12(a), where it is clear that the fits (lines) are a good representation of the data (symbols). This fitting improved the result in that the uncertainty of the intensity minima and maxima averaged out in the curve fitting process.

One issue that always arises in oil-film interferometry approaches that attempt to determine spatial distributions of the wall shear stress is the need to locate the leading edge. The fits found above were used to determine the oil-film height at specific times, a series of which is shown in figure 12(b).

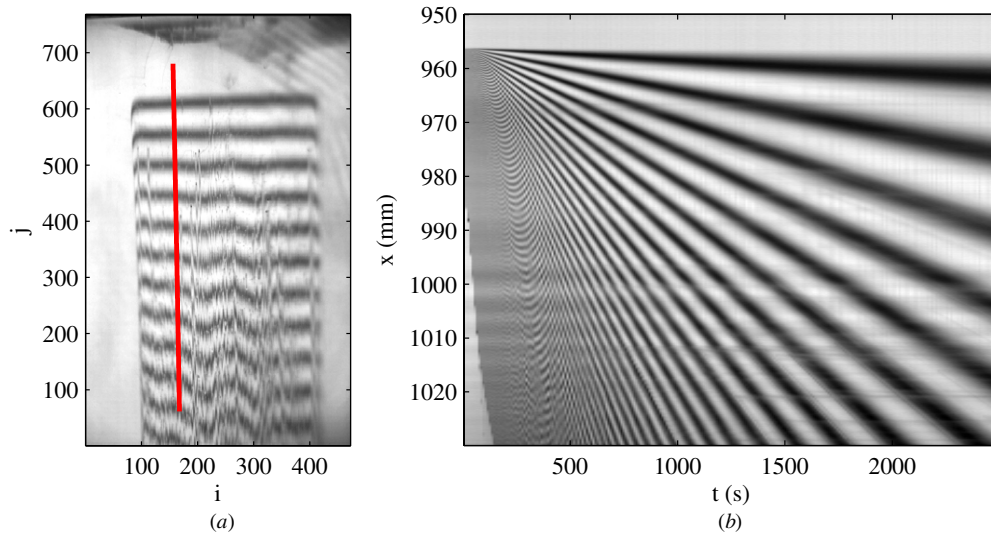


**Figure 9.** Experimental results for the case with a fast startup and a constant tunnel setting (case 1E): (a) an interferogram at one time showing the location from where the interference information was extracted, and (b) the time dependence of the intensity along the lines that were extracted.

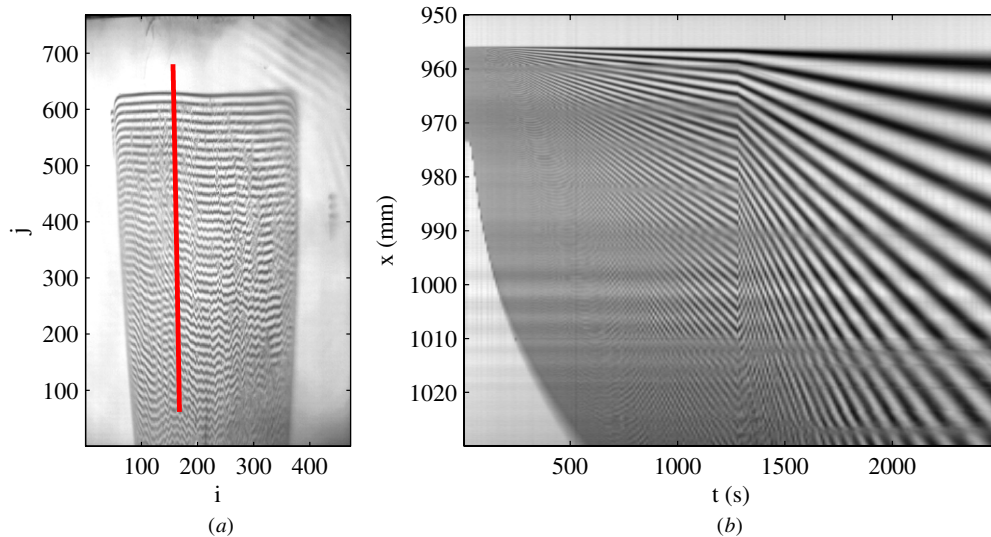


**Figure 10.** Experimental results for the case with two different tunnel settings (case 3E): (a) an interferogram at one time showing the location from where the interference information was extracted, and (b) the time dependence of the intensity along the lines that were extracted.

The three oil-film heights closest to the leading edge at each time were linearly fit, and the results for all times are shown as solid lines in the figure. It is clear that the individual fits all converge pointing to a consistent location of the leading edge. Surprisingly, the fits do not converge at a height of zero as would be expected at the leading edge, but instead have a small finite height. It is believed that this small height is the source of error that has been observed in past studies that considered similar analysis approaches (for example, see [18]). The convergence at finite height is likely due to surface tension effects that have been considered to be relatively minor for practical oil-film implementations. However, the role of surface tension in modifying the oil-film height profile near the leading edge has been discussed [19]. Although the effect is confined to a small region near the leading edge, simply assuming the height is zero at the convergence point

appears to be unacceptable as this likely accounts for the large scatter of wall shear stress values observed in past multi-image implementations. A solution to the problem that is consistent with surface tension being neglected in the present analysis is to simply subtract this small height from the height distribution causing the leading edge location to have a height of zero as required. Having performed this last correction, the wall shear stress was determined using the multi-time inverse method described in section 2.2 (equations (8) and (9)). For this method to work, the shear stress is assumed to remain independent of time for the period chosen for analysis.

In order to provide results with which those of the multi-image approach discussed above can be compared, the single- and dual-image approaches were used to analyze the same data set. The single-image approach thus used height data shown in figure 11, but was restricted to using data from one time. As a



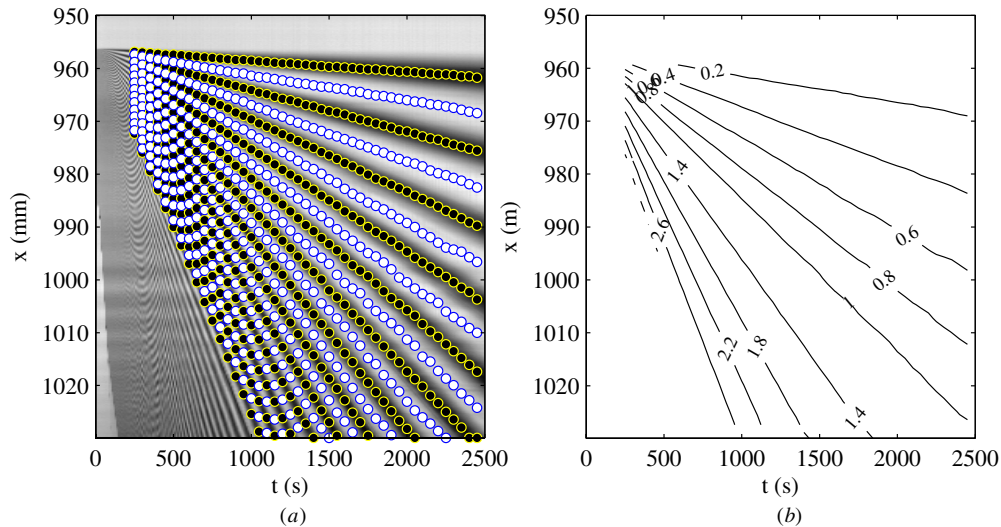


**Figure 11.** Experimental results for a fast startup and a constant tunnel setting (case 1E): (a) interference data overlaid with locations where intensity maxima and minima were identified, and (b) the height distribution (in microns) calculated from the phase information provided by the maxima and minima.

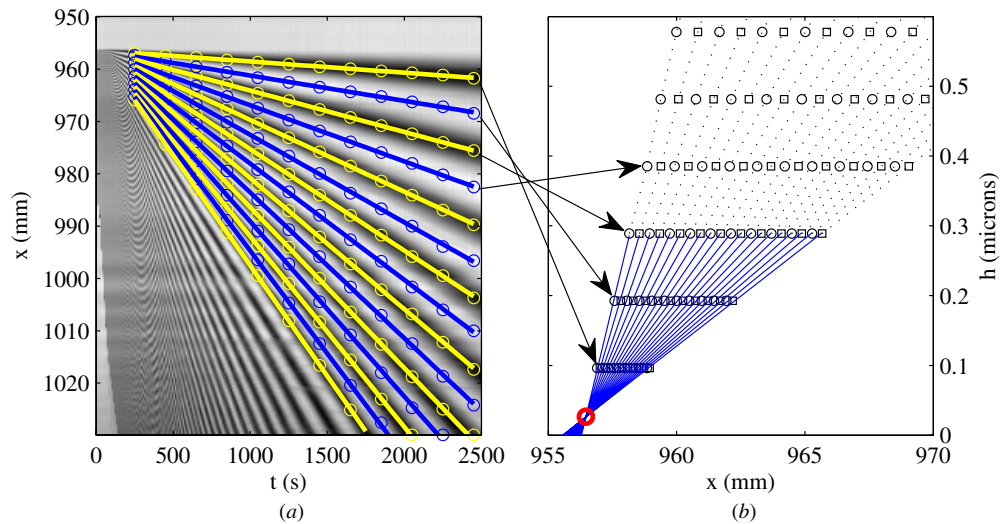


**Figure 12.** Experimental results for a fast startup and a constant tunnel setting (case 1E): (a) interference data overlaid with curve fits of the maxima and minima, and (b) the fit data points near the leading edge used to determine the effective leading edge.

result, fitting in time as performed in the multi-image approach was not possible. To determine the leading edge location, the first three height locations were again used. Since there is no height data from other times, estimation of the leading edge by extrapolating the fit to these points to zero height is used with its associated error. For the single-image approach, this is not critical as the effect of the estimated leading edge location is to impose a wall shear stress at the first node. The resulting height and leading edge information were used with single-image inverse method given by (5) and (6). For the dual-image approach, height data from two times in figure 11 was used. Again, with only two times for which data is used, no fitting in time was performed. However, with two times, an estimate for the leading edge location and 'height' was determined by fitting both height profiles and determining their intersections as was done with the multi-image approach. The corrected height and leading edge location were then used with the multi-

time inverse solution, (8) and (9), to determine the wall shear stress.

### 3. Results

Having discussed the different oil-film analysis approaches to be considered and the data available for analysis, the results of applying different analysis approaches to the different data sets are discussed in this section.

Considering the simulations first, height distributions like that in figure 7 were analyzed. The results for the constant shear stress (case 1C) demonstrated that all the approaches (single-, dual-, and multi-image) yielded the correct result. This is not unexpected as all the assumptions that are made for the single-image analysis approach are exactly met. For the case with different wall shear stress distributions at different times in the simulation (case 2C), the results are somewhat

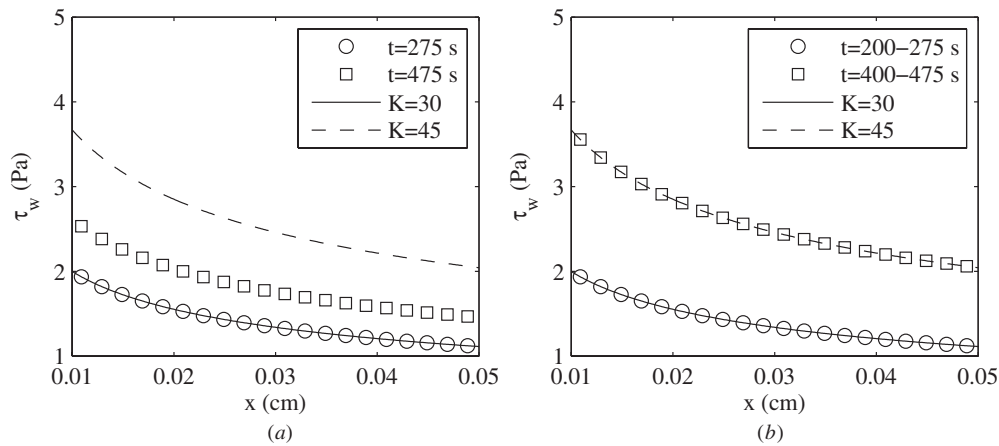


**Figure 13.** Exact wall shear stress distribution and results of analyzing oil-film height data for a Falkner–Skan wedge flow: (a) single-image approach, and (b) multi-image approach.

different. Figure 13 shows the exact results for the two different shear levels as well as the results for (a) the single-image approach and (b) the multi-image approach. As is evident from the figure, the wall shear stress for times less than 300 s is accurately predicted in both cases. This is as expected because, up to 300 s, the wall shear stress is constant. For times greater than 400 s, the multi-image approach yields the correct result, whereas the results from the single-image approach are considerably lower than the exact value. It should be noted that the single-image analysis was performed in wall shear stress (rather than skin friction coefficient) to emphasize the sensitivity of the approach. The wall shear stress at these later times was incorrectly predicted for the single-image approach because the method determined the wall shear stress from information taken during the entire simulation, including times when the wall shear stress distribution was lower in value. In contrast, the multi-image approach yields essentially the known results both before and after the change in wall shear stress. The results for times greater than 300 s are correct for the multi-image approach because only information acquired after the wall shear stress change was used in the analysis. These results are encouraging as they suggest that the approaches behave as expected.

Although the computationally simulated oil-film height confirms that the methods work if given accurate input, actual experimental data are considered next as they likely contain imperfections in the data (imperfect fringes, real test conditions, errors in height calculations, etc) that will affect the results. As a result, the performance of the different analysis methods on the experimental run is considered. The case with a fast startup and constant run conditions thereafter (case 1E) is first considered as all approaches should perform well. Figure 14 shows the results for the three different analysis approaches. It is clear that all three approaches work relatively well here. The dual-image and single-image results are a little noisier than the multi-image case. The results of the single-image approach shown in figure 14(a) at five different times show variability typical of single-image approaches. In particular, the 250 s results appear to be systematically lower than results from other times. Surprisingly, the results using the dual-image approach, shown in figure 14(b) where

the results for four image pairs covering different time intervals are displayed, exhibit the largest variability of the three approaches. The latest time period results (1750 and 2250 s) display a large bias atypical of most oil-film analysis approaches. The most likely sources of this uncertainty are the inaccurate prediction of the leading edge location and height and the error in the integral term of the solution, term A in (7). Term B in (7) does not appear to be responsible for the uncertainty as it should be nearly identical to the term that is found in the multi-image approach. With the exception of a single stray point, the results of the multi-image approach shown in figure 14(c) yielded very consistent results. The time ranges used for the multi-image analysis approach were the same as that used for the dual-image approach. These results, particularly near the leading edge, demonstrate that the multi-image analysis used in this study has addressed problems that plagued earlier analysis methods. The consistency of the methods' results away from the leading edge ( $x > 970$  mm) is also encouraging since they all appear to converge to the same distribution for this case.

A more rigorous test of the different analysis methods is offered by the slow startup case (case 2E). The slow startup would be expected to affect the single-image analysis the most as the startup effects would be included in the wall shear stress result. Due to the formulation of the single-image analysis in terms of skin friction coefficient, the results shown in figure 15(a) are not far from the correct result. The values at the leading edge appear to be high, but the scatter in the data is not great as might be expected. Because the startup period should have less influence the longer the oil film is exposed to the steady conditions after startup, it would be expected that the interference patterns analyzed at later times should produce more accurate results. It is evident that this is not the case here for the reasons discussed above. The results of the two image analysis approach shown in figure 15(b) again exhibit the problems at the leading edge observed in case 1E. The deviations from the expected result near the leading edge are both high and low, which, together with the analysis of the numerical results, point to inaccuracy in the terms suggested above rather than an inherent problem with the approach. The multi-image approach again performs well, and the results

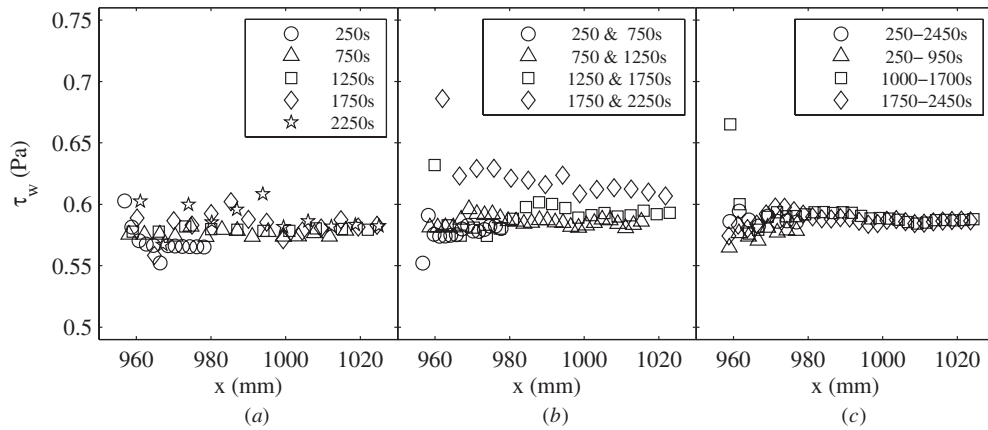


**Figure 14.** Results of different oil-film analysis approaches applied to a run with a fast startup followed by constant run conditions—case 1E: (a) single-image result, (b) dual-image result, and (c) multiple-image result.

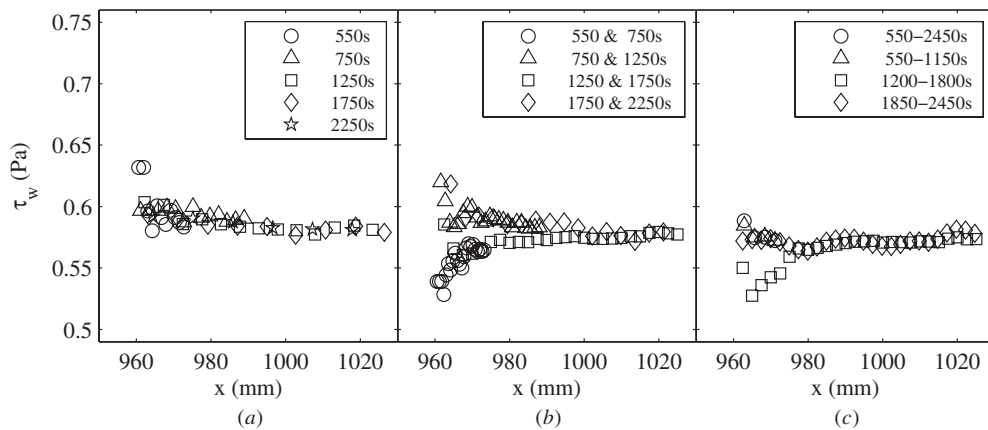


**Figure 15.** Results of different oil-film analysis approaches applied to a run with a long startup followed by constant conditions—case 2E: (a) single-image result, (b) dual-image result, and (c) multiple-image result.

shown in figure 15(c) look very similar to the single-image results, as they should because the run conditions after startup were the same for both cases. For an unknown reason, the results for one time period shown in figure 15(c) (the 1200–1800 s interval) deviates significantly from the others near the leading edge. Despite the differences in the wall shear stress near the leading edge determined by the different analysis approaches, all results converge to similar values away from the leading edge for all times or intervals considered.

The final test case (case 3E) included two distinct test conditions providing perhaps the most challenging case. Figure 16 shows the results where it should be noted that the range of the y-axis is three times that of the previous figures, which affects the relative appearance of data scatter. As shown in figure 16(a), the single-image approach predicts the wall shear stress accurately for times less than ~1300 s during which the wind tunnel is running at the first test condition. Surprisingly, the single-image approach does not perform badly for times >1300 s, a result not expected as the shear stress increases by approximately a factor of four between the two run conditions. This result occurs for this well-behaved boundary layer flow, but should not be expected

to occur in more complicated flows such as a wing changing angle of attack. Although the single-image approach works fairly well, it is noted that the results from 1600–2400 s are biased high and are lowering toward the expected value as time increases. As shown in figure 16(b), the dual-image approach outperforms the single-image approach for the two later time pairs analyzed as the wall shear stress values determined are closer to the expected result that should be the same as that of case 1E. However, the results from the earlier time pairs analyzed before the change in the run conditions (the lower distributions shown in the figure) again display the large leading edge errors observed in the previous two experimental cases. Encouragingly, the multi-image approach appears to perform well again as observed from the results shown in figure 16(c). The two time intervals analyzed before the change in conditions took place yield results consistent with those from the single- and dual-image approaches. Of the different analysis approaches, the multi-image approach applied to data taken during the time interval that falls in the second run condition ( $t > 1300$ ) yields the most consistent and accurate results, conclusively demonstrating the effectiveness of the multi-image approach under such conditions.

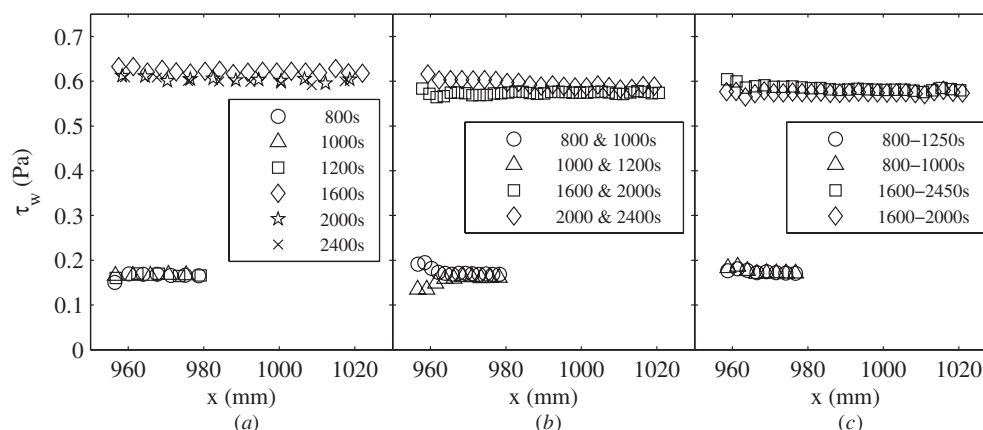


**Figure 16.** Results of different oil-film analysis approaches applied to a run with a short startup followed by two different run conditions—case 3E: (a) single-image result, (b) dual-image result, and (c) multiple-image result.

#### 4. Discussion

The results of applying the three different analysis approaches to both computational and experimental data reveal the strengths and weaknesses of each of the techniques. The single-image approach performs very well if the wall shear stress is relatively constant. Analyzing several lines from an image (assuming some symmetries exist) can be used to reduce the scatter. If the wall shear stress varies significantly during a run, then the two- or multi-image approaches are more appropriate. Although casting the single-image approach in skin friction coefficient produced reasonable results in the boundary layer studied here, it is unlikely that it would perform as well in more complex flows. The dual-image results seem to be quite dependent on the times chosen, with some cases exhibiting large errors near the leading edge as pointed out above. In contrast, the multiple-image approach appears to produce fairly consistent and accurate results, even when conditions have changed substantially. Curve fitting the data from multiple times appears to smooth the oil-film height estimates and thereby reduces the impacts of small height errors on the wall shear stress determined. Although there appears to be small errors in the leading edge region, most of the wall shear stress distributions produced by the multi-image analysis approach produce very smooth results.

#### 5. Conclusions

An assessment of three different approaches for analyzing interferogram images obtained using oil-film interferometry has been performed. Computational simulations of the oil-film height and experiments using oil-film interferometry in a turbulent boundary layer provided the data necessary to assess single-, dual-, and multi-image analysis approaches. The analysis demonstrates that the single-image approach works well when test conditions are achieved rapidly and then are held fairly constant. For cases where the wall shear stress varies more significantly, the dual- and multi-image approaches produce better results. Of the dual- and multi-image approaches, the latter approach appears to be less sensitive to small height errors at the leading edge.

From the results of this study, some recommendation can be made. When its use is appropriate, the single-image analysis approach is recommended for its ease of use. It does not require optical access during a run, which simplifies the setup and acquisition of interferogram images. The reduced amount of data acquired also simplifies data handling. When the single-image approach fails to produce suitable results, the multi-image approach is recommended. Since the setup and acquisition challenges are approximately the same for both dual- and multi-image approaches, the improved results provided by the multi-time approach justify its use despite the additional data and increased analysis complexity. Automation of the multi-image approach, which is desirable, requires high quality interferogram images. Thus, the most suitable technique depends on the exact application, but the different approaches provide options from which the researcher can select thereby providing some flexibility. One additional item that needs further consideration is the effect of surface tension on the leading edge of the oil film. The determination of the leading edge location and the handling of the resulting leading edge 'height' is important for multi-image approaches, and the method used here to consider these issues should be further verified.

#### Acknowledgments

The approaches discussed here were developed by the first author while visiting Chalmers University of Technology. Interactions with Faraz Mehdi and T Gunnar Johansson are gratefully acknowledged.

#### References

- [1] Naughton J W and Sheplak M 2002 Modern developments in shear stress measurement *Prog. Aerospace Sci.* **38** 515–70
- [2] Squire L C 1962 The motion of a thin oil sheet under the boundary layer on a body *Flow Visualization in Wind Tunnels Using Indicators (AGARDograph vol 70)* ed R L Maltby (Paris: NATO AGARD) pp 7–23
- [3] Tanner L H and Blows L G 1976 A study of the motion of oil films on surfaces in air flow, with application to the measurement of skin friction *J. Phys. E: Sci. Instrum.* **9** 194–202



- [4] Siller H A, Perkins R J and Janke G 1993 Image analysis of oil film interferometry—a method of measuring wall shear stress distributions *Flow Visualization and Image Analysis* ed F T M Nieuwstadt (Dordrecht: Kluwer) pp 71–80
- [5] Mateer G G, Monson D J and Menter F R 1996 Skin-friction measurements and calculations on a lifting airfoil *AIAA J.* **34** 231–6
- [6] Garrison T J and Ackman M 1998 Development of a global interferometer skin-friction meter *AIAA J.* **36** 62–68
- [7] Naughton J W and Liu T 2007 Photogrammetry in oil-film interferometry *AIAA J.* **45** 1620–9
- [8] Pailhas G, Barricau P, Touvet Y and Perret L 2009 Friction measurement in zero and adverse pressure gradient boundary layer using oil droplet interferometric method *Exp. Fluids* **47** 195–207
- [9] El-Gammal M, Naughton J W and Hangan H 2010 Drag force balance of a blunt and divergent trailing-edge airfoil *J. Aircr.* **47** 345–8
- [10] Naughton J W, Viken S and Greenblatt D 2006 Skin friction measurements on the NASA hump model *AIAA J.* **44** 1255–65 (also *AIAA Paper* 2004-2607, June 2004)
- [11] Johansson T G, Mehdi F, Shiri F and Naughton J W 2005 Skin friction measurements using oil film interferometry and laser Doppler anemometry *AIAA Paper* 2005-4673
- [12] Naughton J W, Schabron B, Hind M D and Alvi F 2011 Improved wall shear stress measurements on a supersonic microjet impingement surface *AIAA Paper* 2011-1096
- [13] Driver D M 2003 Application of oil-film interferometry skin-friction measurement to large wind tunnels *Exp. Fluids* **34** 717–25
- [14] Drake A and Kennelly R A Jr 1999 In-flight skin friction measurements using oil film interferometry *J. Aircr.* **36** 723–5
- [15] Fernholz H H, Janke G, Schober M, Wagner P M and Warnack D 1996 New developments and applications of skin-friction measuring techniques *Meas. Sci. Technol.* **7** 1396–409
- [16] Naughton J W and Brown J L 1996 Surface interferometric skin-friction measurement technique *AIAA Paper* 96-2183
- [17] Driver D M and Drake A 2008 Skin-friction measurements using oil-film interferometry in NASA's 11-foot transonic wind tunnel *AIAA J.* **46** 2401–7
- [18] Naughton J W 2008 Multiple-image oil film interferometry *AIAA Paper* 2008-0268
- [19] Brown J L and Naughton J W 1999 The thin oil film equation *NASA-TM* 1999-208767 (Washington DC: NASA-Ames Research Center)
- [20] Born M and Wolf E 1999 *Principles of Optics* 7th edn (expanded) (Cambridge: Cambridge University Press) chapter 7, pp 286–359
- [21] Hecht E 1987 *Optics* 2nd edn (Reading, MA: Addison-Wesley) chapter 9, pp 346–61
- [22] White F M 1991 *Viscous Fluid Flow* 2nd edn (New York: McGraw-Hill) pp 242–50